Journal of Zhejiang University-SCIENCE A in press
www.jzus.zju.edu.cn; www.springer.com/journal/11582
E-mail: jzus_a@zju.edu.cn

Research Article
https://doi.org/10.1631/jzus.A2500175

A decomposition method for existing tunnel lining displacement induced by undercrossing: a case study

Yiming FU[1,2], Wenqi DING[1,2], Zhijian ZHAO[3], Wei LONG[3], Yafei QIAO[1,2]✉

[1] *Department of Geotechnical Engineering, College of Civil Engineering, Tongji University, Shanghai 200092, China*
[2] *Key Laboratory of Geotechnical and Underground Engineering of Ministry of Education, Tongji University, Shanghai 200092, China*
[3] *China Railway South Investment Group Co., Ltd., Shenzhen 518000, China*

Abstract: A decomposition method is proposed to divide the field monitoring displacement of tunnel linings into different components induced by dislocation, rotation, and elliptical deformation of the lining rings. Based on this method, a corresponding tunnel lining monitoring plan is also suggested. The key principles of the decomposition are the continuity of longitudinal deformation, the sinusoidal functional relationship between the rotation angle and the longitudinal distance to the cross point, and neglecting the longitudinal joint deformation. The proposed decomposition method was successfully applied to a metro project in China and the decomposed pattern laws were discussed. The decomposed data indicates that the displacement of the lining ring is primarily influenced by elliptical deformation and dislocation, with elliptical deformation having the strongest impact. Moreover, the *z*-direction displacement of the existing tunnels linearly increases with the crossing angle, whereas the affected zone decreases nonlinearly. As for the lining ring rotation angle, its maximum value occurs during a 90° undercrossing scenario, and the rotation angles decrease nonlinearly as the crossing angle diminishes. Furthermore, the rotation angle first increases and then decreases as the distance from the crossing center increases. Temporally, the rotation angles follow a pattern of initial increase followed by gradual reduction. Regarding the ellipticity, the ellipticity increases with the crossing angle but decreases with distance from the crossing center. The findings of this study contribute to improved knowledge of tunnel lining displacement composition and monitoring. Future integration of our computational approach with total station monitoring systems could enable real-time monitoring, calculation, and analysis in tunnel engineering applications.

Unedited

Key words: Displacement decomposition method; Shield tunnel; Field monitoring; Undercrossing; Crossing angle

1 Introduction

Newly constructed tunnels are increasingly crossing under existing metro lines in the development of urban metro systems. Improved understanding of tunnelling-induced displacement of existing tunnels plays a crucial role in construction control, lining design, and reinforcement measures. Therefore, there has been significant research into the patterns of displacement induced by tunnelling, which can be categorized into three groups according to their methodology: analytical solutions, numerical solutions, and field monitoring.

To understand tunnelling-induced disturbances, numerous scholars have proposed theories of displacement for existing tunnels (e.g., Shen et al., 2014; Meng et al., 2025). Some of these displacement theories described the relationship between settlement, rigid body displacement, and overall deformation (Zhang et al., 2016; Soomro et al., 2022). They explored the correlation between settlement time-history development and construction activities, revealing the mechanisms of stress redistribution by quantifying deformation patterns and surface subsidence (e.g., Liu et al., 2021; Fang et al., 2015). However, existing tunnel displacement theories have thus far only analyzed the developmental trends of displacement in existing tunnels. And these theories also have certain accuracy limitations, as some necessary and

✉ Yafei QIAO, yafei.qiao@tongji.edu.cn
Yafei QIAO, https://orcid.org/0000-0001-7567-3988

Received May 8, 2025; Revision accepted Dec. 8, 2025; Crosschecked

© Zhejiang University Press 2025

unavoidable assumptions.

To better replicate tunnel construction disturbances, refined finite element simulations have been conducted. These studies analyzed tunnel deformation characteristics, surrounding soil pressure variations, and surface settlement behavior (e.g., Dias and Kastner, 2013; Yin et al., 2018). Others investigated various influencing factors, such as the effects of crossing angles and vertical distances (z-distance) on lining stress distribution, vault displacement patterns, surface settlement, and lining ring rotation (e.g., Liu et al., 2024; Lai et al., 2020). Finite element simulation results can be correlated with analytical solutions to enable more thorough analysis of the influence of earth pressure on segment deformation, thereby enhancing understanding of the composition of monitored displacements. However, precise finite element simulations require extensive foundational data analysis and prolonged model refinement to achieve accurate results. Moreover, finite element simulations cannot clearly describe issues such as the randomness of strata.

Therefore, analyzing monitoring data stands out as an intuitive method for judgment, providing foundational support for theoretical analysis and finite element simulations (Zhang et al., 2023; Cai et al., 2025). Deformation monitoring has been utilized to investigate construction methods, lining ring damage, deformation behaviors, and surface settlement, among other properties (Huang et al., 2020; Lai et al., 2020). Compared to theoretical and numerical analyses, conclusions derived from deformation monitoring are more accurate and realistic, and thus offer reliable guidance for practical engineering applications (e.g., Li and Chen, 2012; Cao et al., 2018). However, deformation monitoring also exhibits a certain degree of dispersion, which complicates data analysis.

Under the disturbances from tunnelling, an existing tunnel lining may settle, rotate, or deform, resulting in a complex displacement pattern. Although field monitoring data can provide more accurate values of displacement, methods to separate the displacement into different underlying patterns are still in development. Therefore, it is important to be able to effectively distinguish and quantify these components, so as to accurately analyze the settlement of the lining ring and the opening of the segmental joint. Extensive research has investigated the displacement decomposition of lining rings. These include theoretical formulas incorporating rotation and dislocation mechanisms, and theoretical formulas prioritizing shear dislocation with secondary rigid rotation effects. Other studies introduced formulations that simultaneously consider segment rotation and oval deformation, complemented by stress evaluation methods unifying the influences of rotation and strain. For asymmetric loading scenarios, theoretical formulas have also been proposed to characterize the longitudinal bending-shear deformation of shield tunnel segments, improving the precision of displacement prediction in tunnel engineering (e.g., Liu et al., 2013; Wei et al., 2020, 2018). Although some of the aforementioned studies investigated displacement decomposition, they did not fully consider displacement components. Displacement decomposition should integrate the three key factors of rotation, dislocation, and elliptical deformation. Not doing so hinders effective performance evaluation and maintenance strategy development for operational tunnels.

Therefore, in this study we propose a displacement decomposition method for tunnel lining rings that incorporates dislocation, rotation, and elliptical deformation. This method is based on feedback analysis of monitoring data rather than forward theoretical derivations. Methods based on monitoring feedback analysis are more closely aligned with actual engineering conditions and better elucidate the components of lining ring displacement.

Using the proposed decomposition model, a comprehensive analysis is conducted on the ring displacements of the Shenzhen Metro Line 11 Phase II project. Furthermore, the decomposed displacement data were examined to investigate the influence of crossing angle and vertical clearance (Z-distance) on existing tunnel settlement, lining ring rotation, and elliptical deformation. This study enhances the understanding of lining ring displacement components, thereby aiding real-time monitoring and early warning systems, and laying a theoretical foundation for the advancement of digital twin technology in tunnel engineering.

Unedited

The rest of this work is structured as follows. The displacement decomposition methodology will be explained in detail in Section 2. Section 3 will introduce the engineering context for application of the method, and Section 4 will present analysis of the displacement decomposition results and summarize the identified disturbance patterns.

2 Displacement decomposition method

The monitored displacement of a tunnel lining is the combined result of dislocation and rotation of lining rings in the longitudinal direction, and elliptical deformation of lining rings in the cross-section. Determining the contribution of each factor to the measured displacement helps us understand the real deformation state of tunnels. Therefore, a new displacement decomposition method is proposed to back-analyze the dislocation, rotation, and elliptical deformation of lining rings.

2.1 Monitoring

Fig. 1 illustrates a suggested location for monitoring points on a tunnel lining. To accurately describe the elliptical deformation of lining rings, five coordinate points are a necessary minimum, which is what is used in this work. The coordinate system is defined as follows: the *x*-axis is oriented perpendicular to the lining ring plane, and is positive along the subway's operational direction. The *y*-axis represents the horizontal direction within the ring plane, and rightward is the positive direction. The *z*-axis corresponds to the vertical direction within the ring plane, and upward is the positive direction. P1 and P4 are positioned at the horizontal diameter extremities, P5 is located at the crown position, and P2 and P3 are positioned at the railroad track alignment. Since tunnel operations and maintenance also require surveillance of rail displacement, using P2 and P3 can effectively reduce the workload associated with data monitoring. The intersection points between the concrete bed and the inner surface of the lining ring are defined as Point 6 (P6) and Point 7 (P7). To minimize the impact of joints within the same lining ring on the displacement analysis, it is important to position at least two monitoring points on a single segment, such as P4 and P5.

The total station is usually set up in the tunnel, and the lining ring measurement point is approximately in the same straight-line direction. The angle between the line of sight and the tunnel axis is very small, causing the *x*-axis displacement in the measurement data to manifest as a small diagonal distance change, and making it difficult to distinguish from the ranging error. Thus, it is difficult for the total station to obtain reliable *x*-axis displacement measurements; the total station can only capture *y*- and *z*-axis displacements at each monitoring point. The symbols and coordinates of the five monitoring points are defined as P_n (y_n^k, z_n^k), and the displacements of the monitoring point are $\triangle y_n^k$ and $\triangle z_n^k$. In this notation, *n* denotes the identification number of the monitoring point, while *k* represents the monitoring number. The formulas for the aforementioned symbols are given in Eqs. (1) and (2).

$$\Delta y_n^k = y_n^k - y_n^0 (n = 1,2,3,4,5) \tag{1}$$

$$\Delta z_n^k = z_n^k - z_n^0 (n = 1,2,3,4,5) \tag{2}$$

$$\Delta y_6^k = -\frac{(\Delta y_3^k - \Delta y_2^k)u_1}{u_2} + \Delta y_2^k \tag{3}$$

$$\Delta z_6^k = -\frac{(\Delta z_3^k - \Delta z_2^k)u_1}{u_2} + \Delta z_2^k \tag{4}$$

$$\Delta y_7^k = \frac{(\Delta y_3^k - \Delta y_2^k)u_1}{u_2} + \Delta y_3^k \tag{5}$$

$$\Delta z_7^k = \frac{(\Delta z_3^k - \Delta z_2^k)u_1}{u_2} + \Delta z_3^k \tag{6}$$

Here, u_1 represents the linear distance between P6 and P2, while u_2 denotes the distance between P2 and P3. Based on the symmetric configuration of the monitoring system, the distance between P6 and P2 is maintained as equal to the distance between P7 and P3. y_n^0 represents the initial *y*-coordinate of the monitoring point P_n. Due to the high stiffness of the concrete foundation bed, it can be considered a rigid structure. Therefore, the displacements at P6 and P7 can be determined by applying Eqs. (3) – (6).

Unedited

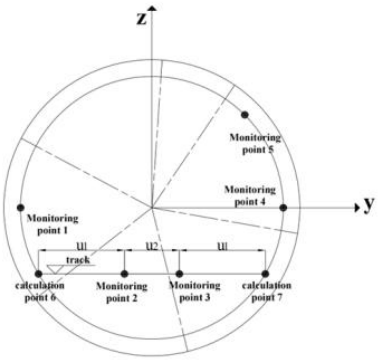

Fig. 1 Schematic of the locations of the monitoring points

2.2 Displacement decomposition mode

Fig. 2 presents a schematic representation of the displacement decomposition methodology. The displacement characteristics of existing tunnel lining systems can be decomposed into three primary components: dislocation, rotation, and elliptical deformation. Regarding dislocation, all five monitoring points on the lining ring have identical horizontal ($\triangle y_n^k$') and vertical ($\triangle z_n^k$') displacement components, maintaining their relative positions throughout the movement. Considering rotational displacement, each monitoring point has a vertical displacement component ($\triangle z_n^k$'') that is directly proportional to its position relative to the center of rotation, with θ representing the rotation angle, l_n representing the z-directional distance between the monitoring point n and the center of the lining ring before deformation. The magnitude of this vertical displacement can be determined by:

$$\Delta z_n^k'' = l_n - l_n \cdot \cos\theta \tag{7}$$

Structural deformation of the lining ring manifests as position-dependent displacement variations, characterized by distinct horizontal ($\triangle y_n^k$''') and vertical ($\triangle z_n^k$''') components at each monitoring point. Therefore, the horizontal and vertical displacements of the five monitoring points can be decomposed into the following components:

$$\Delta y_n^k = \Delta y_n^k' + \Delta y_n^k''' \tag{8}$$

$$\Delta z_n^k = \Delta z_n^k' + \Delta z_n^k'' + \Delta z_n^k''' \tag{9}$$

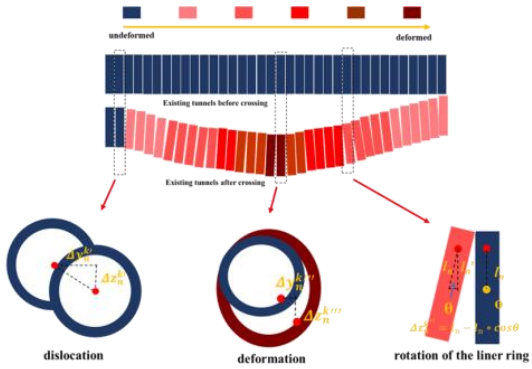

Fig. 2 Displacement decomposition

2.3 Rotation of the lining ring

The difference in the z-directional distance between P4 and P5 is primarily influenced by the rotation of the lining ring and the elliptical deformation. The rotation of the lining ring can be determined by decomposing the change in the z-directional distance between monitoring points P4 and P5. Eq. (10) is used to calculate the variation in the z-directional distance between monitoring points P4 and P5.

$$\Delta z_{45}^k = \Delta z_5^k - \Delta z_4^k \tag{10}$$

Considering the rotation and deformation of three consecutive lining rings as illustrated in Fig. 3 - where the three lining rings are labeled a, b, and c - the rotation angle of the lining ring is denoted as θ_n. Eq. (11) yields the z-directional distance between P4 and P5 before deformation (l_{45}):

$$l_{45} = l_5 - l_4 \tag{11}$$

Consequently, the difference in the z-directional distance between P4 and P5 can be expressed as follows:

$$\Delta z_{45}^k = (l_{45} + l_{45n-d}^k)\cos\theta - l_{45} \tag{12}$$

Where l_{45n-d}^k represents the increment in l_{45} resulting from the elliptical deformation of the lining ring.

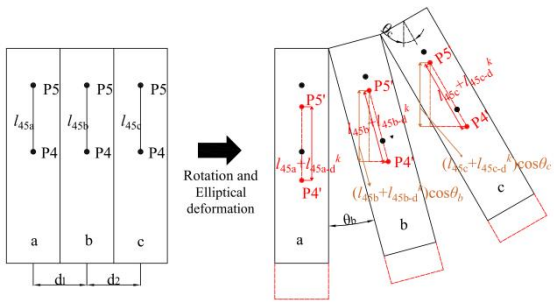

Unedited

Fig. 3 The combined displacement due to rotation and deformation

When an existing tunnel is subjected to a disturbance, the rotation angle at the center of the disturbance is 0°, and the rotation curve of the existing tunnel is continuous. The rotation angle of the lining rings as a function of distance between the disturbance center and the far endpoint (where the rotation angle returns to 0°) can be approximated as a sinusoidal curve (Zhang, 2020; Zhang et al., 2022). Therefore, to facilitate the decomposition of the rotation and oval deformation of the lining rings, the following assumptions are made:

1) The rotation angle of the lining ring at the crossing center of the existing tunnel is 0°, as seen for lining ring a in Fig. 3.

2) The rotation angle of the lining ring is a sinusoidal function of the distance to the crossing center, and its derivative is a cosine function. As illustrated in Fig. 3, the rotation angles of lining rings a, b, and c follow sinusoidal functions for their distances to the crossing centers.

Considering the constraining effect between adjacent lining rings, the $l^k_{45\mathrm{n-d}}$ of lining rings a, b, and c is a continuous function:

$$l^k_{45\text{b-d}} = \frac{d_1 l^k_{45\text{b-c}} + d_2 l^k_{45\text{b-a}}}{d_1 + d_2} \tag{13}$$

Eq. (14) is used to calculate the distance between the disturbance center and the far endpoint, where the rotation angle returns to 0° (Zhang et al., 2022):

$$S = 0.9 \cdot h \cdot \tan(45^\circ + \frac{\varphi}{2}) \tag{14}$$

Here, S represents the distance from the disturbance center to the far endpoint where the rotation angle returns to 0°, and h is the difference in burial depth between the existing tunnel and the new tunnel. The secant slope between two points on the curve is approximately equal to the tangent slope at the midpoint of the two points, as expressed by the following:

$$\frac{\left.\frac{\partial\theta}{\partial d}\right|_{d=\frac{d_1}{2}}}{\left.\frac{\partial\theta}{\partial d}\right|_{d=\frac{d_2}{2}+d_1}} = \frac{\frac{\theta_\mathrm{b}}{d_1}}{\frac{\theta_\mathrm{c}-\theta_\mathrm{b}}{d_2}} = \frac{\cos(\frac{\frac{d_1}{2}}{S}\bullet\pi)}{\cos(\frac{\frac{d_2}{2}+d_1}{S}\bullet\pi)} \tag{15}$$

By substituting the rotation angles and deformations of lining rings b and c into Eq. (15), Eqs. (16) and (17) can be derived:

$$\Delta z^k_{45\mathrm{b}} = (l_{45\mathrm{b}} + l^k_{45\text{b-d}})\cos\theta_b - l_{45} \tag{16}$$

$$\Delta z^k_{45\mathrm{c}} = (l_{45\mathrm{c}} + l^k_{45\text{c-d}})\cos\theta_\mathrm{c} - l_{45} \tag{17}$$

By solving the system of equations (Eqs. (13)–(17)) using MATLAB, the rotation angle of lining ring b can be determined. Subsequently, through application of the same computational method to solve the systems of equations for the following two rings, the rotation angle of lining ring c can be obtained. By repeating this calculation process along the tunnel, the rotation angles of all the lining rings can be determined sequentially. Once the rotation angles of the lining rings are determined, $\triangle z^{k\prime\prime}_n$ can be derived using Eq. (7).

2.4 Dislocation of the lining ring

The track is supported by a concrete bed beneath the rails. Under the condition that no cracks develop between the concrete bed and the lining ring, the concrete bed can be considered as a rigid body structure; consequently, the concrete bed is resistant to deformation. The monitoring data at points P2 and P3 are similar, and thus one can assume that the two monitoring points on the concrete bed only undergo dislocation and rotation of the lining ring. The rotation of the lining ring does not affect the *y*-direction dislocation, instead only influencing the *z*-direction dislocation. Therefore, the dislocation magnitude of the lining ring can be obtained by eliminating the rotational effects from the average displacement changes at monitoring points P2 and P3. The values calculated from Eqs. (18) and (19) represent the internal structural dislocation of the lining ring.

$$\Delta y^{k\prime}_n = \frac{\Delta y^k_2 + \Delta y^k_3}{2} \tag{18}$$

Unedited

$$\Delta z_n^{k\prime} = \frac{\Delta z_2^k + \Delta z_3^k}{2} - l_2 \sin(\theta_n^k) \tan(\frac{\theta_n^k}{2}) \tag{19}$$

2.5 Elliptical deformation of the lining ring

Using Eqs. (8) and (9), $\triangle z_n^{k\prime\prime\prime}$ and $\triangle y_n^{k\prime\prime\prime}$ can be computed accordingly. Based on this result, the post-deformation elliptical configuration of the lining ring (including the geometric parameters of its major and minor axes) can be precisely determined through fitting analysis. This analysis, performed in MATLAB, utilizes the spatial coordinates of P1, P4, P5, P6, and P7, where the coordinates of P6 and P7 are derived from the coordinates of P2 and P3 using Eqs. (20) – (23). The degree of elliptical deformation of the lining ring is then calculated using Eq. (24).

$$y_6 = -\frac{(y_3 - y_2)u_1}{u_2} + y_2 \tag{20}$$

$$z_6 = -\frac{(z_3 - z_2)u_1}{u_2} + z_2 \tag{21}$$

$$y_7 = \frac{(y_3 - y_2)u_1}{u_2} + y_3 \tag{22}$$

$$z_7 = \frac{(z_3 - z_2)u_1}{u_2} + z_3 \tag{23}$$

$$e = \frac{r_1 - r_2}{2R} \tag{24}$$

where e is the ellipticity, r_1 is the length of the long axis, r_2 is the length of the short axis, and R is the radius of the lining ring.

2.6 Summary and discussion

The proposed calculation method holds true under the following assumptions:

1) The rotation angle of the lining ring at the crossing center of the existing tunnel is 0°.

2) The rotation angle of the lining ring is a sinusoidal function of the distance to the crossing center, and its derivative is a cosine function.

3) The deformation caused by longitudinal joints in the lining rings can be neglected.

4) Considering the constraining effect between adjacent lining rings, the l_{45n-d}^k of adjacent lining rings is a continuous function.

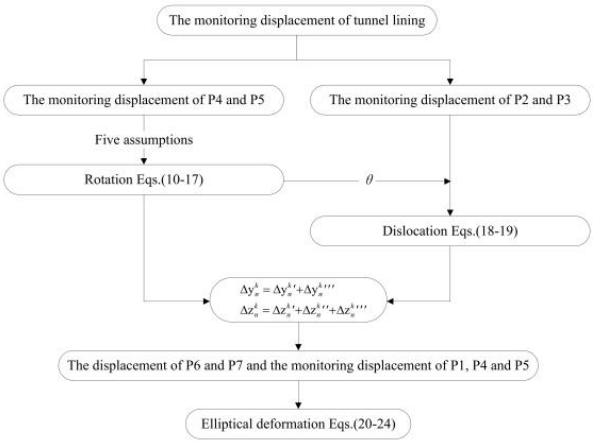

Fig. 4 A flowchart describing the displacement decomposition method

Fig. 4 presents a calculation flowchart of the above displacement decomposition method. The steps of the method are as follows: First, from the displacement monitoring data at points P4 and P5, the rotation angle of the lining ring is calculated based on the deformation-rotation compatibility equations, z-direction displacement difference decomposition equations, and the mentioned assumptions. However, it should be noted that engineering uncertainties and stochastic factors can lead to errors in calculating the rotation angles. Then, after calculating the average value of the displacement monitoring data at points P2 and P3, the dislocation of adjacent lining rings is determined by removing the influence of the lining ring rotation. Finally, the rotation angles and dislocation of the lining ring are substituted into Eqs. (8) and (9) to calculate the deformation components of the displacements of the five nodes on the lining ring. Then, the ellipticity of the lining ring is obtained through curve fitting in MATLAB.

3. Project overview

3.1 Route of the tunnel

The Shenzhen Metro Line 11, Phase II Project, which lies between the Eighth Affiliated Hospital of Sun Yat-sen University Station and Gangxia North Station, comprises a left tunnel with a total length of about 1,054 m and a right tunnel extending about 1,105 m. Fig. 5 illustrates the route of the project and the monitoring areas for the existing tunnels. The right tunnel of Line 11 first perpendicularly crosses

Unedited

the left and right tunnels of Line 1, which is followed by a crossing at an angle of 14° with the exit tunnel of Line 14, and finally, a parallel crossing with the Line 14 exit tunnel. For the left tunnel of Line 11, the sequence begins with a crossing of the Line 14 exit tunnel at an angle of 47°, followed by a crossing of the Line 14 admission tunnel at 24°, and finally with a perpendicular crossing of the left and right tunnels of Line 1. Since there are many tunnels in this section, diverse crossing angles, complex geological conditions, and Line 1 has been in operation for a long time, the application, in the Shenzhen Metro Line 11 Phase II Project, of the proposed displacement decomposition model holds significant research value.

Shenzhen Metro Line 1 was constructed in 2004 using the cut-and-cover method, while Shenzhen Metro Line 14 was constructed in 2022 using the shield tunneling method. These lines differ in two key aspects: 1) Construction Method: The cut-and-cover method used for Line 1 typically results in a structure with lower overall stiffness and integrity compared to the modern shield-tunneled segments of Line 14. This makes Line 1 more sensitive structurally to disturbances from below. 2) Ground Conditions and Burial Depth: Line 1 has a shallower burial depth than Line 14. The influence of the new tunnel (Line 11) on the deeper Line 14 is relatively larger than that in Line 1. In terms of the impact on the shallower Line 1, the presence of the deeper Line 14 itself acts as a mitigating factor, effectively reducing the disturbance transferred from the new construction to Line 1 above.

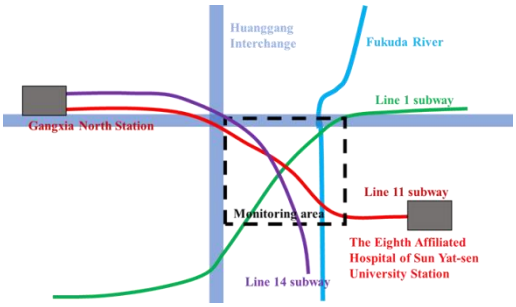

Fig. 5 The locations and monitoring zones of existing and new tunnels

3.2 Construction program

The Line 11 tunnel employs an Earth Pressure Balance (EPB) shield machine, characterized by an excavation diameter of 6.48 m. The tunnel is situated at varying overburden depths ranging from 10.8 to 13.5 m. The shield tunnel lining segment has an inner diameter of 5.5 m, an outer diameter of 6.2 m, and a width of 1.5 m, and the tunnel lining ring is composed of six segments. The segments are installed using a staggered joint configuration to enhance the structural integrity. The EPB shield machine operates under controlled parameters: the soil chamber pressure is maintained at approximately 290 kPa to ensure stability of the face, while the grouting pressure is regulated at around 320 kPa to optimize ground consolidation and minimize disturbance. The cutter head torque is controlled at approximately 2,000 kPa to maintain efficient excavation performance while preventing excessive ground disturbance. The chamber pressure, grouting pressure, and cutterhead torque are dynamically adjusted in response to changes in the shield machine's tunneling depth.

3.3 Geological conditions

Fig. 6 presents a stratigraphic cross-section illustrating the geological structure and geotechnical parameters along vertical profiles; more details on the geotechnical parameters are listed in Table 1. The geological profile above the shield tunnel - in descending stratigraphic order - is comprised of the following distinct layers: stockpile soil, silty sand, grit, gravelly clayey soil, fully weathered granite, strongly weathered granite, moderately weathered granite, and weakly weathered granite. Line 14 primarily traverses through silty sand and grit, and Line 1 is mainly situated in fully weathered granite. Line 11 predominantly passes through mixed granite formations, intermittently encountering less competent strata such as gravelly clay, coarse sand, and medium sand layers.

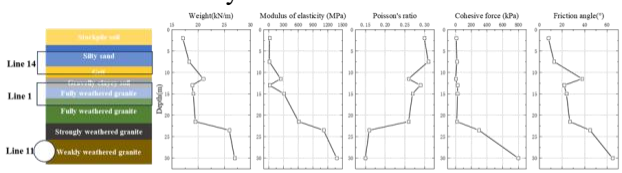

Fig. 6 The soil profile and geotechnical parameters along the depth direction

Table 1 Geotechnical parameters

Soil Layer Name	Thickness	Modulus of	Poisson's	Cohesive	Friction	Weight

Unedited

	(m)	Elasticity (MPa)	Ratio	Force (kPa)	Angle (°)	(kN/m)
Stockpile soil	2	20	0.3	12	8	17.1
Silty sand	5.5	15	0.31	20	13	18.3
Grit	4	244	0.26	4	38	21
Gravelly clayey soil	1.5	20	0.29	27	22	18.9
Fully weathered granite	2	312	0.27	26	24	19.1
Strongly weathered granite	6.5	611	0.26	18	27	19.5
Moderately weathered granite	2	1,118	0.16	300	45	26
Weakly weathered granite	-	1,384	0.15	800	65	27

3.4 Monitoring program

To better apply the proposed displacement decomposition method, the following monitoring point arrangement was implemented on Line 1 and Line 14 of the Shenzhen Metro. The monitoring points of Line 1 and Line 14 are illustrated in Fig. 7. The spacing between monitoring sections ranges from 4.5 m to 10 m, with an appropriate densification of monitoring points established in the crossing area. There are 18 total monitoring sections distributed along both the left and right tunnels of Line 1, complemented by 20 monitoring sections on Line 14's entrance tunnel and 37 monitoring sections on its exit tunnel. Using the displacement decomposition method proposed in this study, each monitoring section was instrumented with five monitoring points, as illustrated in Fig. 7a.

Unedited

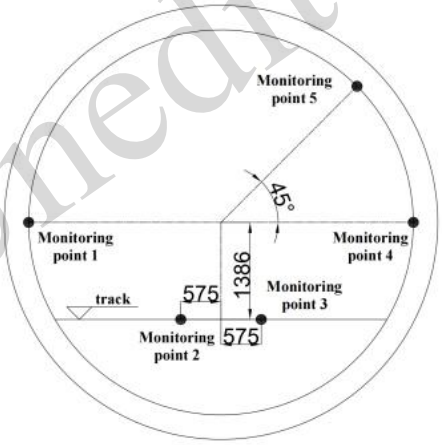

(a) Layout of monitoring points in the lining ring (mm)

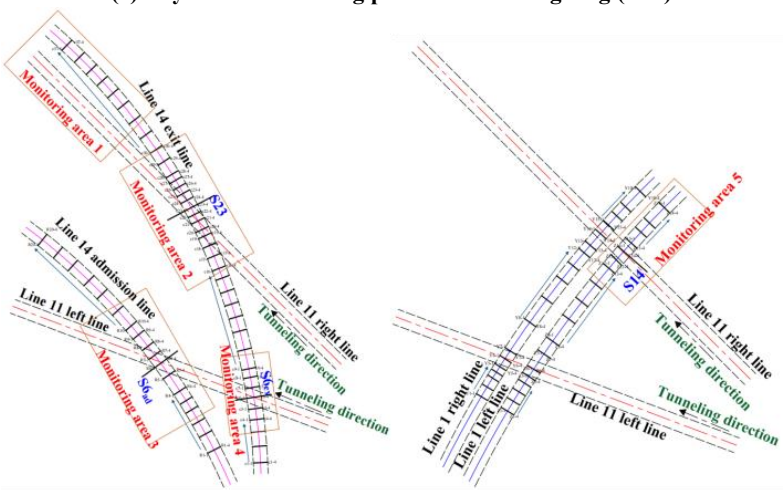

Line 11 crossing of Line 14 and monitoring area (m)

Line 11 crossing of Line 1 and monitoring area (m)

(b) The monitoring areas of Line 1, Line 11, and Line 14

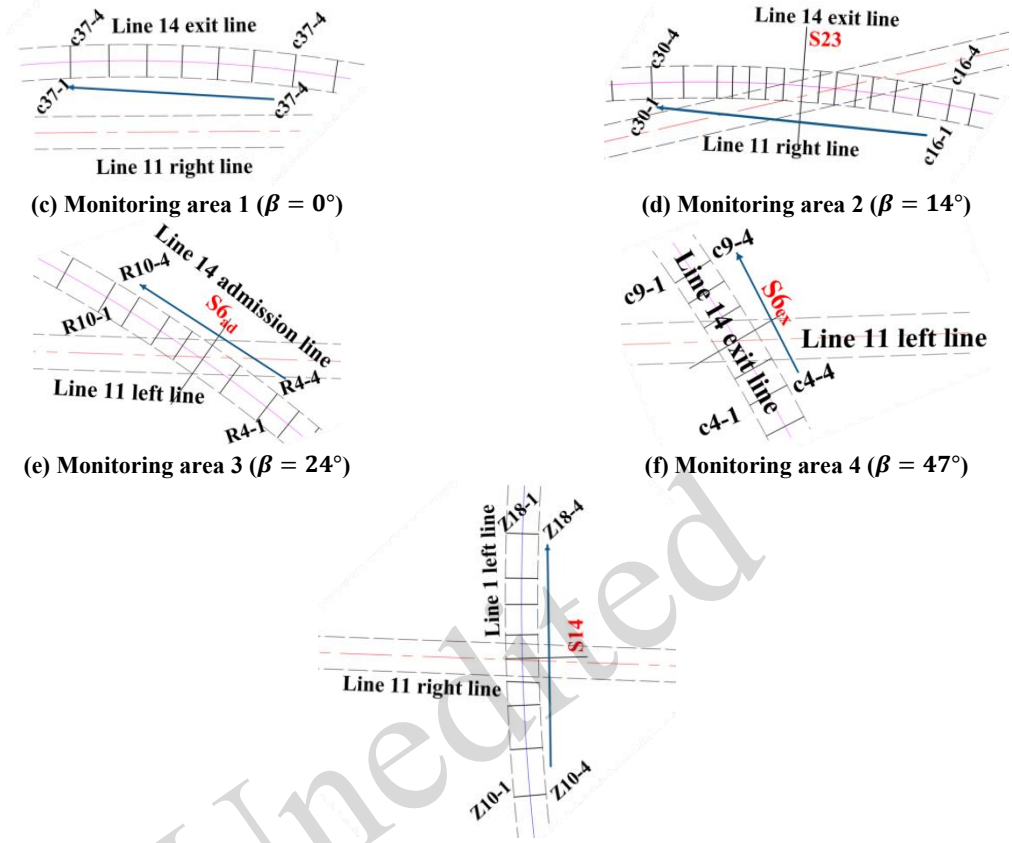

(c) Monitoring area 1 ($\beta = 0°$)

(d) Monitoring area 2 ($\beta = 14°$)

(e) Monitoring area 3 ($\beta = 24°$)

(f) Monitoring area 4 ($\beta = 47°$)

(g) Monitoring area 5 ($\beta = 90°$)

Fig. 7 Monitoring points and monitoring areas

Unedited

The designated monitoring area was located at the intersection zone where Metro Line 11 crosses both Line 1 and 14. Table 2 summarizes the key parameters of the five monitoring areas within the crossing zone, including the crossing angle, vertical (*z*-direction) tunnel separation distance, monitoring duration, cross-section number at the crossing center, and the crossing time. The monitoring areas include:

- Monitoring area 1: the area where the right tunnel of Line 11 crosses the exit tunnel of Line 14 in parallel, as illustrated in Fig. 7c.
- Monitoring area 2: the area where the right tunnel of Line 11 crosses the exit tunnel of Line 14 at an angle of 14°, and S_{23} is the crossing section, as illustrated in Fig. 7d.
- Monitoring area 3: the area where the left tunnel of Line 11 crosses the admission tunnel of Line 14 at an angle of 24°, and S_{6ad} is the crossing section, as illustrated in Fig. 7e.
- Monitoring area 4: the area where the left tunnel of Line 11 crosses the exit tunnel of Line 14 at an angle of 47°, and S_{6ex} is the crossing section, as illustrated in Fig. 7f.
- Monitoring area 5: the area where the right tunnel of Line 11 perpendicularly crosses the left tunnel of Line 1, and S_{14} is the crossing section, as illustrated in Fig. 7g.

Table 2 Key parameters of the five monitoring areas

Monitoring areas	Crossing angle β(°)	Z-direction distance (m)	Monitoring duration	Cross-section number at the crossing center	Crossing time
Monitoring area 1	0	25	June 7 to June 16	/	/
Monitoring area 2	14	25	May 20 to May 30	23	May 26

Monitoring area 3	24	25	April 19 to May 1	6	April 27
Monitoring area 4	47	25	April 12 to April 25	6	April 22
Monitoring area 5	90	17.2	May 20 to June 2	14	May 26

4. Monitoring data and displacement decomposition results

4.1 Settlement of the lining ring

The settlements of the existing tunnel at the five monitoring sections are presented in Fig. 8. It is important to note that the settlement herein does not mean the dislocation between individual lining rings as in Section 4.1. The settlement of the lining ring concrete bed is affected by both the rotation angle of the lining ring and the dislocation of the lining ring. As the monitoring sections are not uniformly distributed across every lining ring, only the settlement of the lining ring can be analyzed. Therefore, for the present problem, the settlement calculations follow:

$$\Delta s_n^k = \frac{\Delta z_2^k + \Delta z_3^k}{2} \tag{25}$$

In this section, downward displacement (towards the new tunnel) is defined as positive. The influence range of the new tunnel was determined to be the distance between the point where the settlement becomes zero and the front and the back of the crossing center. When the shield machine is located more than 50 m away from the crossing center, its influence on the central section becomes negligible. With the shield advancing at a rate of approximately 5 m per day, the z-direction settlement of the lining ring was analytically reset to zero about 10 days before the machine arrived at the central cross-section for convenience (Zhang et al., 2022).

Unedited

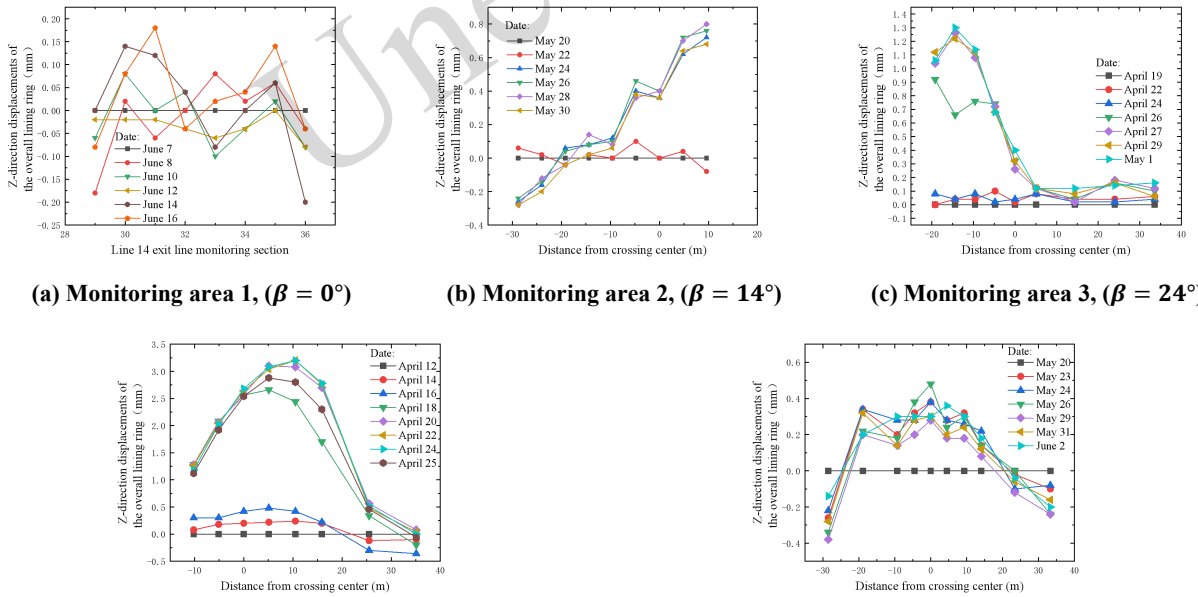

(a) Monitoring area 1, ($\beta = 0°$) **(b) Monitoring area 2, ($\beta = 14°$)** **(c) Monitoring area 3, ($\beta = 24°$)**

(d) Monitoring area 4, ($\beta = 47°$) **(e) Monitoring area 5, ($\beta = 90°$)**

Fig. 8 z-direction settlements of the lining ring

Fig. 8 shows the time-history curves of z-direction settlement of the existing tunnel for undercrossing at different angles. The maximum z-direction settlement is: 0.15 mm for parallel crossing, 0.8 mm at 14°, 1.3 mm at 24°, and 3.0 mm at 47°. The relationship between z-direction settlement, influence range, and crossing angle is presented in Fig. 9. The results demonstrate that the maximum settlement increases linearly with crossing angle, while the influence range decreases

in a nonlinear fashion as the crossing angle increases.

Fig. 8a demonstrates that the settlements along different sections of Line 14 exhibit uniform temporal variations. Consequently, the disturbances induced by the parallel undercrossing in the existing tunnel display no discernible spatiotemporal patterns, instead manifesting as random fluctuations. In contrast, the small-angle undercrossings produce significantly disturbed patterns in the existing tunnel structure. Thus, parallel undercrossing is more relevant to the continuity of *z*-direction settlement of the existing tunnel, while perpendicular undercrossing is more relevant to new tunnel crossings.

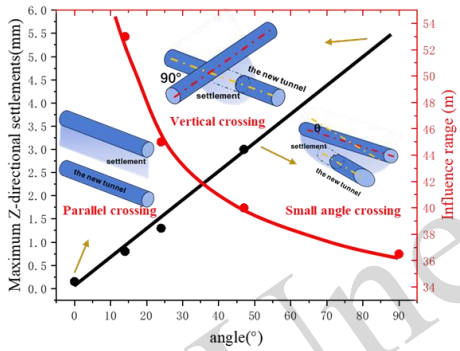

Fig. 9 The relationship between *z*-direction settlement, influence range, and crossing angle

When the crossing angle was 47°, prior to crossing, the *z*-direction settlement in the section was nearly zero. During crossing, the *z*-settlement rapidly increased to 3.0 mm, which was followed by a slight decrease to 2.75 mm after the crossing was complete, as illustrated in Fig. 8d. This 8.3% rebound demonstrates the partial recovery effect of grouting and other stabilization measures on existing tunnel deformation. As the crossing angle reaches 90°, -0.4 mm of settlement occurs at locations which are 30 m away, indicating that vertical undercrossing induces upward deformation (reverse buckling) of the existing tunnel at these distant positions, as illustrated in Fig. 8e.

4.2. Rotation of the lining ring

Theoretically, a parallel undercrossing does not induce lining ring rotation in existing tunnels. Therefore, our rotational analysis focuses exclusively on monitoring areas 2-5. Fig. 10 illustrates the rotation angles of the lining rings, calculated by Eqs. (10)-(17), in monitoring areas 2-5 at different monitoring times; here, positive values indicate leftward rotation from the crossing center, and negative values denote rightward rotation toward the crossing center. When the crossing angle is 14°, the maximum rotation angle of the lining ring reaches 0.75×10^{-3} degrees. This increases to 1.07×10^{-3} degrees at 24°, 1.01×10^{-3} degrees at 47°, and peaks at 1.11×10^{-3} degrees for the 90° crossing. Fig. 11 depicts this nonlinear relationship between crossing angle and maximum lining ring rotation angle.

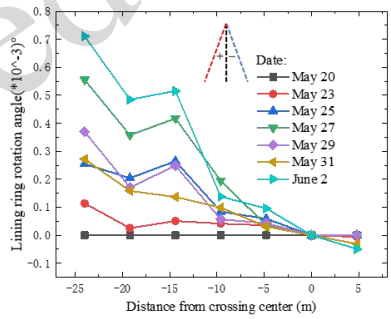

(a) Monitoring area 2, ($\beta = 14°$)

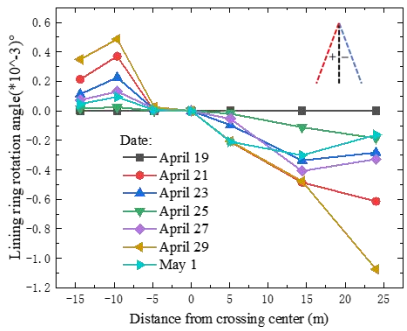

(b) Monitoring area 3, ($\beta = 24°$)

Unedited

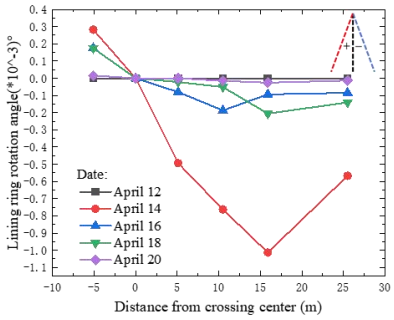

(c) Monitoring area 4, ($\beta = 47°$)

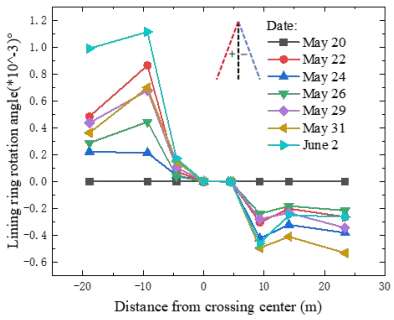

(d) Monitoring area 5, ($\beta = 90°$)

Fig. 10 The rotation angles of the lining rings in monitoring areas 2-5

Analysis of the 24° undercrossing case (Fig. 10b) reveals the spatiotemporal evolution of the lining ring rotation angle. The lining ring rotation angle initially increases and then decreases with increasing distance from the undercrossing center. The rotation angle exhibits a rapid initial increase followed by a gradual decrease.

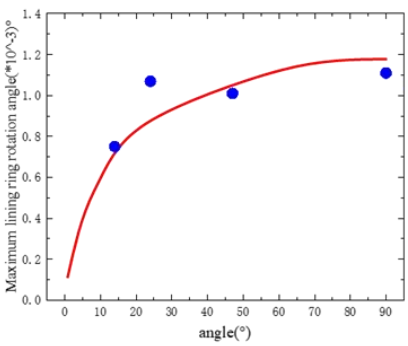

Fig. 11 The relationship between the crossing angle and the maximum lining ring rotation angle

4.3. Elliptical deformation of lining rings

To investigate the variation in ellipticity in a single lining ring under different crossing angles over time, this section presents the ellipticity versus time curves for S_{23} in monitoring area 2, S_{6ad} in monitoring area 3, S_{6ex} in monitoring area 4, and S_{14} in monitoring area 5, as shown in Fig. 12. These curves demonstrate two distinct patterns, which are determined by the magnitude of the crossing angle. For a small crossing angle, the ellipticity initially increases rapidly before stabilizing. During the stabilization phase, significant fluctuations in ellipticity are observed (see Fig. 12(a) and 12(b)). In contrast, for a large crossing angle, the ellipticity first rises sharply and then gradually stabilizes. During the stabilization phase, fluctuations in the ellipticity are relatively minor (see Fig. 12(c) and 12(d)). When the crossing angle is small, the influence of the newly constructed tunnel persists for an extended period. In contrast, a large crossing angle leads to a shorter-lived impact. Therefore, the duration of influence emerges as the predominant factor governing the magnitude of the ellipticity fluctuations.

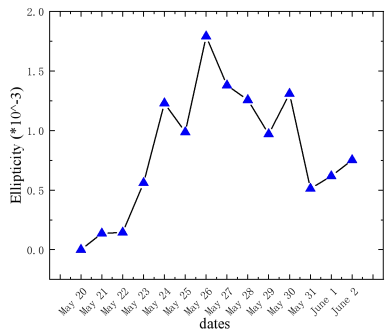

(a) Monitoring area 2, ($\beta = 14°$)

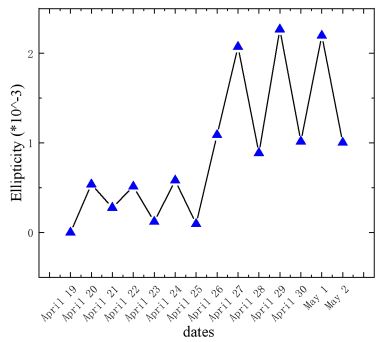

(b) Monitoring area 3, ($\beta = 24°$)

Unedited

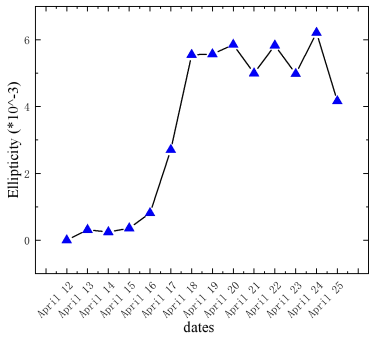

(c) Monitoring area 4, ($\beta = 47°$)

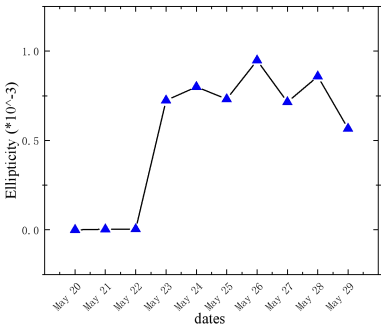

(d) Monitoring area 5, ($\beta = 90°$)

Fig. 12 The ellipticity versus time curves of the crossing sections in four monitoring areas

Based on the time-dependent ellipticity curves of multiple lining rings, Fig. 13 illustrates the spatial distribution of ellipticity and its evolution over time. The maximum measured ellipticity values are 1.7‰, 3.0‰, and 6.5‰ at crossing angles of 14°, 24°, and 47°, respectively. These results demonstrate that the maximum ellipticity increases with crossing angle. However, as depicted in Fig. 13d, when the crossing angle is 90°, the maximum ellipticity is 1.0‰, which is lower than the values under smaller crossing angles. When the crossing angle is 90°, the existing tunnel analyzed under the small-angle crossing is Line 1, not Line 14. However, based on the engineering context, significant differences exist between Line 14 and Line 1 in terms of construction methods, ground conditions, and the distance between the existing and newly constructed tunnels. Therefore, the maximum ellipticity depends not only on the crossing angle but also on such variables.

When the crossing angles are 47° and 90°, as illustrated in Fig. 13d and Fig. 13e, respectively, the ellipticity of the lining rings decreases with increasing distance to the crossing center. However, this spatial distribution does not hold for the 14° and 24° undercrossing cases. While generally the ellipticity variation decreases with increasing distance, the unusual pattern identified in this case was primarily caused by grouting activities compensating for ground loss, resulting in fluctuations in the lining ring deformation. In addition, construction randomness and other uncertainties likely influenced this behavior. Thus, the ellipticity variation in the lining rings is influenced not only by tunnel excavation, but also by factors such as grouting conditions and shield machine attitude adjustments.

Unedited

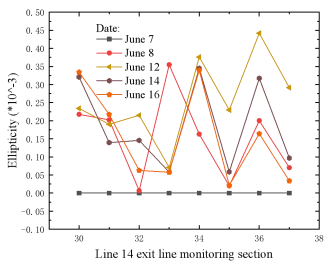

(a) Monitoring area 1, ($\beta = 0°$)

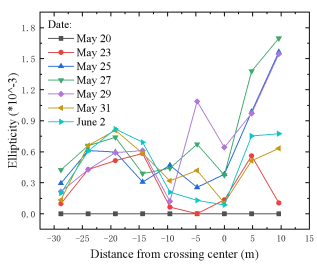

(b) Monitoring area 2, ($\beta = 14°$)

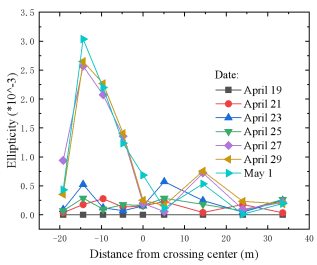

(c) Monitoring area 3, ($\beta = 24°$)

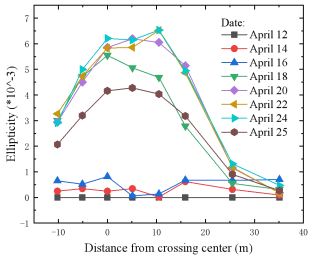

(d) Monitoring area 4, ($\beta = 47°$)

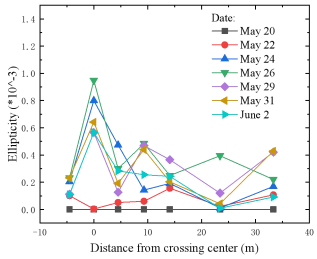

(e) Monitoring area 5, ($\beta = 90°$)

Fig. 13 The variation curve of ellipticity for each section

Subsequently, based on the elliptical deformation fitting results of the lining rings, the relationship between the relative position of the new tunnel and the existing tunnel, as well as the direction of the elliptical major axis can be analyzed. In this section, a case in which the right line of Line 11 perpendicularly crosses the left line of Line 1 is selected for analysis. As illustrated in Fig. 14, when Line 11 is excavated up to cross-section a, the major axis of the elliptical deformation in the calculated left-line section of Line 1 points towards cross-section a of Line 11. Next, as Line 11 advances to cross-section b, the major axis of the elliptical deformation in the left-line section of Line 1 deviates from its original orientation, shifting towards cross-section b of Line 11. This indicates that the long axis of the ellipse of the existing tunnel section is often oriented towards the excavation face of the new tunnel.

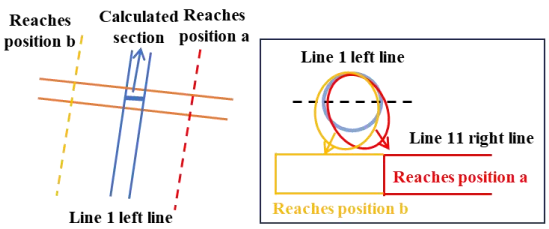

Fig. 14 The long axis of the tunnel section ellipse points

4.4. Discussion

The proposed displacement decomposition method can be effectively applied to tunnel crossings at various angles, enabling rapid decomposition of lining ring displacements into three components: dislocations, rotations, and deformations. Leveraging this method enables more accurate assessments of the tunnel's bearing state, thereby facilitating selection of appropriate emergency countermeasures for different risk scenarios. Future integration of this computational approach with total stations could enable real-time monitoring, calculation, and analysis. Nevertheless, there are several limitations caused by engineering uncertainties, random factors, and excessive deformation that should be acknowledged. The inverse analysis of known lining ring rotations and displacements demonstrates that the rotation angle follows a sinusoidal function with respect to distance. However, engineering uncertainties and stochastic factors inevitably introduce errors into the rotation angle calculations. For one, the lining rings are assumed to be homogeneous circular rings in our analysis. But when excessive deformation occurs, this assumption may not hold true, and errors may be introduced into the ellipticity calculations. For areas with significant deformation, targeted high-precision monitoring measures should be implemented. Our analysis also assumes that there is no deformation in the tracks and the concrete bed. However, this assumption becomes invalid when excessive lining ring deformation occurs, particularly if cracks develop between the concrete bed and lining rings.

5. Conclusions

This paper proposes a method for decomposing lining ring displacements in the context of shield tunneling. This decomposition method can process total station monitoring data through separation into three components: dislocation, rotation, and deformation. Because the approach is based on feedback analysis of monitoring data, it is more closely aligned with actual engineering conditions

Unedited

and better facilitates understanding of the components of lining ring displacement. The proposed method was effectively utilized to analyze the displacements of existing tunnels caused by the undercrossing of new tunnels in Phase II of the Shenzhen Metro, Line 11.

Based on certain assumptions, including the functional relationship between rotation angle and distance, continuity of deformation, and homogeneous circular ring properties, the rotation angle was calculated using deformation-rotation compatibility equations and *z*-direction displacement difference decomposition equations. Then, the dislocation of the lining ring was obtained by removing the rotation effect from the average displacement of the track monitoring points. Subsequently, the deformation of the lining ring was derived by eliminating both the rotation and dislocation components from the measured lining ring displacements. Finally, the calculated values were matched with the coordinates of the monitoring points, and the ellipticity of the lining ring was obtained through curve fitting in MATLAB.

Z-direction displacement was revealed as the primary factor affecting the displacement of the lining ring. The *z*-direction displacement of the existing tunnels linearly increases with larger crossing angles, whereas the affected zone decreases nonlinearly. During the undercrossings, the *z*-direction settlement initially rises rapidly and then gradually decreases due to construction measures such as grouting.

Across different crossing angles, the maximum lining ring rotation angle occurs during a 90° undercrossing scenario, and the rotation angles decrease nonlinearly as the crossing angle diminishes. Under constant crossing angle, the spatiotemporal pattern involves the rotation angle increasing first and then decreasing as the distance from the crossing center increases. Temporally, the rotation angles follow a pattern of initial increase followed by gradual reduction.

Spatially, the lining ring ellipticity increases with crossing angle but decreases with distance from the crossing center. Temporally, two distinct patterns of ellipticity variation were observed. Although both models exhibit similar trends, different crossing angles significantly impact the post-stabilization amplitude fluctuations. Additionally, the long axis of the elliptical deformation consistently points towards the excavation face of the new tunnel.

In future work, more data will be collected and processed using displacement decomposition methods to derive statistical patterns. This will establish relationships between construction parameters and deformation, which may ultimately help guide construction practices. Moreover, future integration of our computational approach with total station monitoring systems could enable real-time monitoring, calculation, and analysis of tunnel lining displacement. This study provides a robust foundation for real-time early warning systems, offering theoretical support for developing digital twins in tunnel engineering applications. Nonetheless, assumptions behind the proposed model may still introduce errors into the results. Subsequent efforts should therefore also focus on refining these assumptions to enhance the computational accuracy.

Unedited

Acknowledgments

The authors would like to thank the National Natural Science Foundation of China (52090083)、the China Railway Southern Technology Development Program and Yunnan Provincial Science and Technology Department Science and Technology Program(No.202303AA080003) for funding the research work in this paper.

Author contributions

Yiming Fu processed the corresponding data and wrote the first draft of the manuscript. Wenqi Ding, Zhijian Zhao and Wei Long helped to organize the manuscript. Yafei Qiao revised and edited the final version.

References

Baishya R, Choudhury D, 2025. Dynamic analysis of the effect of vertical clearance on an existing perpendicular crossing tunnel in soil. Transportation Infrastructure Geotechnology, 12(4) https://doi.org/10.1007/s40515-025-00586-9

Cai YQ, Ying HK, Wang J, et al., 2025. Impact of engineering geological environment on sensor-enabled piezoelectric geocable (spgc) monitoring performance-accelerated aging test. Engineering Geology, 349 https://doi.org/10.1016/j.enggeo.2025.107970

Cao L, Fang Q, Zhang D, et al., 2018. Subway station

construction using combined shield and shallow tunnelling method: Case study of gaojiayuan station in beijing. Tunnelling and Underground Space Technology, 82:627-635. https://doi.org/10.1016/j.tust.2018.09.010

Chen RP, Lin XT, Kang X, et al., 2018. Deformation and stress characteristics of existing twin tunnels induced by close-distance epbs under-crossing. Tunnelling and Underground Space Technology, 82:468-481. https://doi.org/10.1016/j.tust.2018.08.059

Dias D, Kastner R, 2013. Movements caused by the excavation of tunnels using face pressurized shields - analysis of monitoring and numerical modeling results. Engineering Geology, 152(1):17-25. https://doi.org/10.1016/j.enggeo.2012.10.002

Ding N, Zhou Y, Li D, et al., 2024. Real-time deformation monitoring of large diameter shield tunnel based on multi-sensor data fusion technique. Measurement, 225 https://doi.org/10.1016/j.measurement.2023.114061

Fang Q, Zhang D, Li Q, et al., 2015. Effects of twin tunnels construction beneath existing shield-driven twin tunnels. Tunnelling and Underground Space Technology, 45:128-137. https://doi.org/10.1016/j.tust.2014.10.001

Fang Q, Tai Q, Zhang D, et al., 2016. Ground surface settlements due to construction of closely-spaced twin tunnels with different geometric arrangements. Tunnelling and Underground Space Technology, 51:144-151. https://doi.org/10.1016/j.tust.2015.10.031

Fang Y, Ni D, Cai F, et al., 2024. 3d numerical investigation of the interaction between interchange tunnels at different angles. Heliyon, 10(5) https://doi.org/10.1016/j.heliyon.2024.e27394

Galli G, Grimaldi A, Leonardi A, 2004. Three-dimensional modelling of tunnel excavation and lining. Computers and Geotechnics, 31(3):171-183. https://doi.org/10.1016/j.compgeo.2004.02.003

Huang L, Ma J, Lei M, et al., 2020. Soil-water inrush induced shield tunnel lining damage and its stabilization: A case study. Tunnelling and Underground Space Technology, 97 https://doi.org/10.1016/j.tust.2020.103290

Huang M, Zhou Z, 2023. Explicit solution analysis of tunnel excavation under existing pipelines on the double-parameter foundation. Journal of Safety and Environment, 23(6):1852-1858.

Kumar A, Chauhan VB, Kumar P, et al., 2024. Interplay of tunnel geometry and shallow foundation stability in rock: Comparative insights into failure modes. International Journal of Geomechanics, 24(9) https://doi.org/10.1061/ijgnai.Gmeng-9815

Lai H, Zheng H, Chen R, et al., 2020. Settlement behaviors of existing tunnel caused by obliquely under-crossing shield tunneling in close proximity with small intersection angle. Tunnelling and Underground Space Technology, 97 https://doi.org/10.1016/j.tust.2019.103258

Lee IM, Nam SW, 2001. The study of seepage forces acting on the tunnel lining and tunnel face in shallow tunnels. Tunnelling and Underground Space Technology, 16(1):31-40. https://doi.org/10.1016/s0886-7798(01)00028-1

Li PF, Zhao Y, Zhou XJ, 2016. Displacement characteristics of high-speed railway tunnel construction in loess ground by using multi-step excavation method. Tunnelling and Underground Space Technology, 51:41-55. https://doi.org/10.1016/j.tust.2015.10.009

Li X, Chen X, 2012. Using grouting of shield tunneling to reduce settlements of overlying tunnels: Case study in shenzhen metro construction. Journal of Construction Engineering and Management, 138(4):574-584. https://doi.org/10.1061/(asce)co.1943-7862.0000455

Li X, Du S, Zhang D, 2012. Analysis on influence of new shield tunneling on closely spaced parallel tunnel. Chinese Journal of Underground Space and Engineering, 8(5):1065-1069,1074.

Li Z, Chen Z, Yang Y, et al., 2024. Deformation characteristics of existing tunnels induced by above-crossing quasi-rectangular shield tunnel. Transportation Geotechnics, 45 https://doi.org/10.1016/j.trgeo.2024.101227

Lin C-G, Zhang Z-M, Wu S-M, et al., 2013. Key techniques and important issues for slurry shield under-passing embankments: A case study of hangzhou qiantang river tunnel. Tunnelling and Underground Space Technology, 38:306-325. https://doi.org/10.1016/j.tust.2013.07.004

Liu S, He M, Liu J, 2021. Deformation analysis on the existing shield tunnel obliquely crossed by new tunnel. Chinese Journal of Underground Space and Engineering, 17(1):263-272.

Liu X, Fang Q, Zhang D, et al., 2019. Behaviour of existing tunnel due to new tunnel construction below. Computers and Geotechnics, 110:71-81. https://doi.org/10.1016/j.compgeo.2019.02.013

Liu X, Zhang R, Fang Q, et al., 2024. Subgrade settlements of existing railway lines and operational parameters of shield machine induced by twin shield tunnel excavations: A case study. Journal of Central South University, 31(1):272-287. https://doi.org/10.1007/s11771-023-5447-9

Lo KY, Ramsay JA, 1991. The effect of construction on existing subway tunnels - a case-study from toronto (reprinted from canadian tunneling canadien, 1990). Tunnelling and Underground Space Technology, 6(3):287-297. https://doi.org/10.1016/0886-7798(91)90140-y

Sharifzadeh M, Kolivand F, Ghorbani M, et al., 2013. Design of sequential excavation method for large span urban tunnels in soft ground - niayesh tunnel. Tunnelling and Underground Space Technology, 35:178-188. https://doi.org/10.1016/j.tust.2013.01.002

Shen SL, Wu HN, Cui YJ, et al., 2014. Long-term settlement

Unedited

behaviour of metro tunnels in the soft deposits of shanghai. Tunnelling and Underground Space Technology, 40:309-323. https://doi.org/10.1016/j.tust.2013.10.013

Soomro MA, Samo SR, Saand A, et al., 2022. Numerical parametric study of settlement and load transfer mechanism of pile group due to twin stacked tunnelling with different construction sequences. European Journal of Environmental and Civil Engineering, 26(3):1064-1096. https://doi.org/10.1080/19648189.2019.1695678

Wanchai T, Cho G-C, 2005. Tunneling in bangkok-two case studies

tunnelling in bangkok - two case studies. Journal of Korean Tunnelling and Underground Space Association, 7(2):59-69.

Wei G, Yang B, Wu H, et al., 2020. Research on longitudinal deformation of existing shield tunnel caused by shield tunneling. Chinese Journal of Underground Space and Engineering, 16(6):1754.

Wei X, Hong W, Wei G, et al., 2018. Rotation and shearing dislocation deformation of subway tunnels due to adjacent ground stack load. Chinese Journal of Rock Mechanics and Engineering, 37(5):1281-1289.

Wham BP, Argyrou C, O'rourke TD, 2016. Jointed pipeline response to tunneling-induced ground deformation. Canadian Geotechnical Journal, 53(11):1794-1806. https://doi.org/10.1139/cgj-2016-0054

Wu H-N, Shen S-L, Liao S-M, et al., 2015. Longitudinal structural modelling of shield tunnels considering shearing dislocation between segmental rings. Tunnelling and Underground Space Technology, 50:317-323. https://doi.org/10.1016/j.tust.2015.08.001

Yin ML, Jiang H, Jiang YS, et al., 2018. Effect of the excavation clearance of an under-crossing shield tunnel on existing shield tunnels. Tunnelling and Underground Space Technology, 78:245-258. https://doi.org/10.1016/j.tust.2018.04.034

Zhang M, Zhang J, Wu Y, et al., 2019. Analysis of double-line shield tunnel over-crossing subway tunnel in completely weathered rock formation. China Civil Engineering Journal, 52(9):100-108.

Zhang P, Chen R-P, Wu H-N, et al., 2020. Ground settlement induced by tunneling crossing interface of water-bearing mixed ground: A lesson from changsha, china. Tunnelling and Underground Space Technology, 96 https://doi.org/10.1016/j.tust.2019.103224

Zhang Q, Xia T, Ding Z, et al., 2016. Effect of nearby undercrossing tunneling on the deformation of existing metro tunnel and construction control. Rock and Soil Mechanics, 37(12):3561-3568.

Zhang X, Tan H, Liu Z, et al., 2023. Study on the influence of subway tunnel induced by under-crossing tunnel based on monitor data in shenzhen, china. Sustainability, 15(17) https://doi.org/10.3390/su151713232

Zhang ZW, Zheng G, Cheng XS, et al., 2024. Analytical approach for longitudinal deformation of shield tunnels considering bending-shear-torsional effects of circumferential joints. Tunnelling and Underground Space Technology, 152 https://doi.org/10.1016/j.tust.2024.105946

Zhang XH, 2020. Study on the Effects of Excavation on the Stress and Deformation of Shield Tunnel Structures.

Zhang ZG, Cheng ZX, Zhang MX, et al., 2022. Study on Longitudinal Structural Step Deformation of Shield Tunneling Under Existing Tunnels Considering Lining Permeability. Journal of Highway and Transportation Engineering, 35(11):180-194. https://doi.org/10.19721/j.cnki.1001-7372.2022.11.017

Electronic supplementary materials

Tables S1-S4

Unedited